ISSN 1674-1056
http://cpb.iphy.ac.cn
http://iopscience.iop.org/cpb
中国物理 B
Chinese Physics
中国物理
Chinese Physics B

Single boron atom anchored on graphitic carbon nitride nanosheet (B/g-C_2N) as a photocatalyst for nitrogen fixation: A first-principles study

Hao-Ran Zhu(祝浩然), Jia-Liang Chen(陈嘉亮), and Shi-Hao Wei(韦世豪)
Citation: Chin. Phys. B, 2021, 30 (**8**): 083101. DOI: 10.1088/1674-1056/abe3f6
Journal homepage: http://cpb.iphy.ac.cn; http://iopscience.iop.org/cpb

What follows is a list of articles you may be interested in

A strategy to improve the electrochemical performance of Ni-rich positive electrodes: Na/F-co-doped $LiNi_{0.6}Mn_{0.2}Co_{0.2}O_2$

Hui Wan(万惠), Zhixiao Liu(刘智骁), Guangdong Liu(刘广东), Shuaiyu Yi(易帅玉), Fei Gao(高飞), Huiqiu Deng(邓辉球), Dingwang Yuan(袁定旺), and Wangyu Hu(胡望宇)
Chin. Phys. B, 2021, 30 (**7**): 073101. DOI: 10.1088/1674-1056/abeeeb

Discontinuous transition between Zundel and Eigen for $H_5O_2^+$

Endong Wang(王恩栋), Beien Zhu(朱倍恩), Yi Gao(高嶷)
Chin. Phys. B, 2020, 29 (**8**): 083101. DOI: 10.1088/1674-1056/ab973d

Re effects in model Ni-based superalloys investigated with first-principles calculations and atom probe tomography

Dianwu Wang(王殿武), Chongyu Wang(王崇愚), Tao Yu(于涛), Wenqing Liu(刘文庆)
Chin. Phys. B, 2020, 29 (**4**): 043103. DOI: 10.1088/1674-1056/ab6587

Single-doped charged gold cluster with highly selective catalytic activity for the reduction of SO_2 by CO: First-principles study

Yan-Ling Hu(胡燕玲), Hao-Ran Zhu(祝浩然), Shi-Hao Wei(韦世豪)
Chin. Phys. B, 2019, 28 (**11**): 113101. DOI: 10.1088/1674-1056/ab4cdd

Interface properties and electronic structures of aromatic molecules with anhydride and thio-functional groups on Ag (111) and Au (111) substrates

Wei-Qi Yu(余维琪), Hong-Jun Xiao(肖红君), Ge-Ming Wang(王戈明)
Chin. Phys. B, 2019, 28 (**10**): 103101. DOI: 10.1088/1674-1056/ab4276

Single boron atom anchored on graphitic carbon nitride nanosheet (B/g-C_2N) as a photocatalyst for nitrogen fixation: A first-principles study*

Hao-Ran Zhu(祝浩然)[1,2], Jia-Liang Chen(陈嘉亮)[1], and Shi-Hao Wei(韦世豪)[1,†]

[1] *Department of Microelectronic Science and Engineering, School of Physical Science and Technology, Ningbo University, Ningbo* 315211, *China*
[2] *College of Electronic Information and Optical Engineering, Nankai University, Tianjin* 300350, *China*

(Received 24 December 2020; revised manuscript received 4 February 2021; accepted manuscript online 8 February 2021)

It is essential to explore high efficient catalysts for nitrogen reduction in ammonia production. Based on the first-principles calculation, we find that B/g-C_2N can serve as high performance photocatalyst in N_2 fixation, where single boron atom is anchored on the g-C_2N to form B/g-C_2N. With the introduction of B atom to g-C_2N, the energy gap reduces from 2.45 eV to 1.21 eV and shows strong absorption in the visible light region. In addition, N_2 can be efficiently reduced on B/g-C_2N through the enzymatic mechanism with low onset potential of 0.07 V and rate-determining barrier of 0.50 eV. The "acceptance-donation" interaction between B/g-C_2N and N_2 plays a key role to active N_2, and the BN_2 moiety of B/g-C_2N acts as active and transportation center. The activity originates from the strong interaction between $1\pi 1\pi^*$ orbitals of N_2 and molecular orbitals of B/g-C_2N, the ionization of 1π orbital and the filling of $1\pi^*$ orbital can increase the N≡N bond length greatly, making the activation of N_2. Overall, this work demonstrates that B/g-C_2N is a promising photocatalyst for N_2 fixation.

Keywords: first-principles calculation, N_2 reduction, catalysts, electronic structure, reaction mechanisms, reaction paths

PACS: 31.15.A–, 34.70.+e, 73.22.–f, 82.20.Kh **DOI:** 10.1088/1674-1056/abe3f6

1. Introduction

Ammonia (NH_3) is not only an important chemical in agriculture and industry fields but also a potential energy storage intermediate due to its high energy density, safe and environment ecofriendly.[1–4] Currently, the industrial NH_3 production mainly relies on the Haber–Bosch process with Fe- or Ru-based catalysts, which involves harsh conditions (typically 300–500 °C and 200–300 atm), yielding roughly 500 million tons per year, accompanied by the heavy energy consumption, necessary H_2 feedstock from fossil fuel and a large number of greenhouse gases emission.[3,5,6] Thus, it is of great significance to develop a green and sustainable strategy for NH_3 production.[7] The proton-assisted photocatalytic or electrocatalytic N_2 reduction reaction (NRR), ideally under ambient conditions using renewable solar and wind energy, has been proposed as a promising alternative for nitrogen fixation and ammonia production, which stem from N_2 biological fixation with nitrogenase enzymes in bacteria that perform nitrogen fixation at room temperature and atmospheric pressure.[3,6,8–11] For instance, photo(electro)catalytic NRR can be directly driven by the sunlight.[4,6] Thus, these two strategies are highly promising for achieving clean, carbon-free and sustainable NH_3 production from N_2.

Up to date, numerous catalysts have been fabricated for N_2 fixation, such as Ru, graphene, MXene, metal oxides.[12–17] Although NRR catalysts based on noble metals (e.g., $Au_{27,28}$, Ru_{29}, Rh_{30}) show favorable activity, the scarcity and high cost hinder the widespread application. Compared to metal based catalysts, metal-free catalysts can possess excellent activity, long durability, and intrinsic advantages of low cost and environmental friendliness.[14,16,18–35] Recently, boron-doped graphene shows that NH_3 production rate can reach up to 9.8 $\mu g \cdot h^{-1} \cdot cm^{-2}$ with a high faradic efficiencies of 10.8% at 0.5 V versus reversible hydrogen electrode in aqueous solutions at ambient conditions.[14] B_4C nanosheet achieves a high NH_3 yield of 26.57 $\mu g \cdot h^{-1} \cdot mg^{-1}$ and a high Faradic efficiency of 15.95% at a potential of −0.75 V in 0.1 M HCl.[16] The development of efficient metal-free catalysts for NRR is of great economic interest and scientific importance. In 2015, a novel 2D layered crystal with uniformly distributed holes, graphitic carbon nitride named g-C_2N was successfully prepared by a simple bottom-up wet chemical method.[36] The native porous structure of g-C_2N makes it the excellent substrate to support single-atom catalysts (SACs). At present, the N-containing big holes could anchor TM atoms tightly to carry out a series of electro-catalytic reaction like hydrogen evolution reaction (HER),[37,38] oxygen evolution reaction (OER)[38,39] and N_2 reduction reaction (NRR).[40] Also, the moderate energy gap make it suitable for the application for photocatalysts.

*Project supported by the National Natural Science Foundation of China (Grant No. 51871126) and the K. C. Wong Magna Fund in Ningbo University.
†Corresponding author. E-mail: weishihao@nbu.edu.cn
© 2021 Chinese Physical Society and IOP Publishing Ltd

In this work, we employ first-principles calculations to design single boron atom anchored on g-C_2N monolayers (B/g-C_2N) and explore their catalytic performance towards N_2 reduction. As is expected, the decoration of B atom on g-C_2N can maintain and enhance slightly the visible light absorption, making the reduction process possibly occur under visible light. In addition, compared to insufficient ability of g-C_2N to adsorb N_2, B/g-C_2N can bind the N_2 strongly, with binding energies of -0.57 eV and -1.40 eV through side-on and end-on patterns, respectively. Surprisingly, the adsorbed N_2 can be further reduced into NH_3 with a rather low onset potential of 0.07 V and Gibbs free energy barrier of 0.50 eV through the enzymatic mechanism. The stability of B/g-C_2N is systematically evaluated and shows that the designed catalyst is very promising to be synthesized.

2. Calculation details

The spin-polarized DFT calculations are performed using the Vienna *ab initio* simulation package (VASP)[43,44] with projector-augmented-wave (PAW) pseudopotentials.[45] The generalized gradient approximation (GGA) in the form of the Perdew–Burke–Ernzerhof (PBE)[38,39] is used for treating the electronic exchange-correction interactions and a cutoff energy of 500 eV for the plane-wave expansion is adopted. The convergence threshold is 10^{-5} eV and 0.01 eV/Å for energy and force, respectively. A vacuum space is larger than 20 Å, which is set to avoid interactions between two periodic units. The single-atom catalyst is modeled by depositing one B atom on $2\times2\times1$ supercell g-C_2N. Brillouin zones are sampled by a Monkhorst–Pack k-point mesh with a $3\times3\times1$ k-point grid. In order to better describe the long-range van der Waals interaction, the DFT-D2 correction[46] proposed by Grimme and co-workers is applied. Hybrid functionals based on the Heyd–Scuseria–Ernzerhof (HSE06) method[47] are employed to obtain the exact band structures and optical absorption spectra. The climbing nudged elastic band (CI-NEB) method[49] as implemented in VTST tools is carried out to search the transition states and saddle points along the reaction pathway, and the activation barriers for electrochemical reaction are calculated using a transferable method reported by Janik *et al.*[49] *Ab initio* molecular dynamics simulation (AIMD) by the Forcite code[50] with isobaric-isothermal (NPT) ensemble is employed to evaluate the thermodynamic stability of the materials, the simulation is run under 1000 K for 100 ps with time step of 2 fs.

The calculations of Gibbs free energy change (ΔG) for each elemental step are based on the computational hydrogen electrode model proposed by Nørskov *et al.*,[51,52] which can be determined as follows:

$$\Delta G=\Delta E+\Delta E_{\mathrm{ZPE}}-T\Delta S+\Delta G_U+\Delta G_{\mathrm{pH}}, \tag{1}$$

where ΔE is the difference between the adsorption energies of a given group; ΔE_{ZPE} and ΔS are the changes in zero point energies and entropy, severally; T is the temperature, which is set to be 298.15 K in this work; ΔG_U is the contributions of electrode potential to shift the free energy ΔG at the applied electrode potential (U); ΔG_{pH} is the free energy correction of pH ($\Delta G_{\mathrm{pH}}=2.303\times k_{\mathrm{B}}T\times\mathrm{pH}\approx0.059\times\mathrm{pH}$), wherein the pH value is set to be zero in this work. The E_{ZPE} and TS for each reaction intermediates can be calculated from the vibrational frequencies, via the following equation:

$$E_{\mathrm{ZPE}}=\frac{1}{2}\sum_{i=1}^{n}h\nu_i, \tag{2}$$

$$TS=TR\sum_{i=1}^{n}\left\{\frac{hc\tilde{\nu}_i}{k_{\mathrm{B}}T\left(\mathrm{e}^{\frac{hc\tilde{\nu}_i}{k_{\mathrm{B}}T}}-1\right)}-\ln\left(1-\mathrm{e}^{-\frac{hc\tilde{\nu}_i}{k_{\mathrm{B}}T}}\right)\right\}, \tag{3}$$

where R, h, c, k_{B}, ν and $\tilde{\nu}$ are gas constant, Planck's constant, light speed, Boltzmann's constant, vibrational frequencies and wave number, respectively. Moreover, only the calculation of zero point energy and entropy of reaction intermediates are needed and the contribution of substrate can be offset. The entropies and zero-point energies of molecules in the gas phase are obtained from the NIST database [http://cccbdb.nist.gov/].

3. Results and discussion

3.1. B-doped g-C_2N

As shown in Fig. 1, due to the fact that the radius of B atom is larger than that of C atom and N atom, four rational types of adsorption site for the adsorption of B atom on g-C_2N are considered: type-1 is located at the linkage site of two nitrogen atoms, type-2 is positioned in the bridge site of C atom, type-3 corresponds to the middle of six-membered ring which including two N atoms and four C atoms, and type-4 is the middle of six-membered ring of carbon atoms. Initially, B atom is added in each kind of adsorption sites. After full optimization of these adsorption structures, the type-2 and type-3 transfer to the type-1, and the corresponding binding energy is calculated to be -4.94 eV. As for the type-4, B atom moves to the bridge site of C atom and also has a negative binding energy of -1.06 eV (Fig. 1). Obviously, the binding energy of type-1 is most favorable in energy. High binding energy and large energy difference of the formation energies between the different adsorption types of the B/g-C_2N provide significant advantages in terms of experimental synthesis, so the following researches focus on the structure of type-1.

The deposition of B atom on g-C_2N can significantly modify its electronic structure. Figure 2 presents the band structures and optical adsorption spectra of pristine g-C_2N and B/g-C_2N. The band gap of g-C_2N is calculated to be 2.45 eV, which is in accordance with the previous theoretical results.[47,48] When B atom is deposited on g-C_2N, an impurity energy level (IEL, shown in Fig. 2(b) with green line) come

from B atom is introduced, which lies in the midst of band gap of g-C_2N. Therefore, the band gap of B/g-C_2N is significant reducing to 1.21 eV, and the non-magnetic g-C_2N will possess the magnetic moment of $1\mu_B$ when B atom interact with two N atoms of g-C_2N (BN_2 moiety, namely moiety-1).

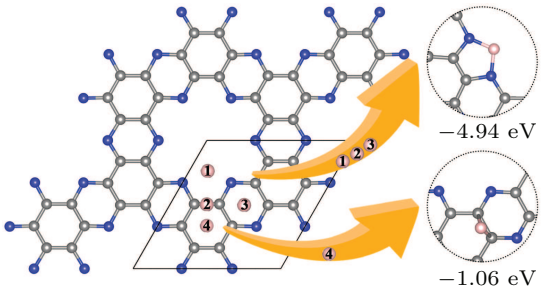


Fig. 1. Initial structures of B atom adsorbed on g-C_2N at different sites (at the left panel), and their optimized structures are illustrated on the right panel. The binding energies are −4.94 eV and −1.06 eV, respectively. The gray, lightpink, and blue balls represent C, B and N atoms, respectively.

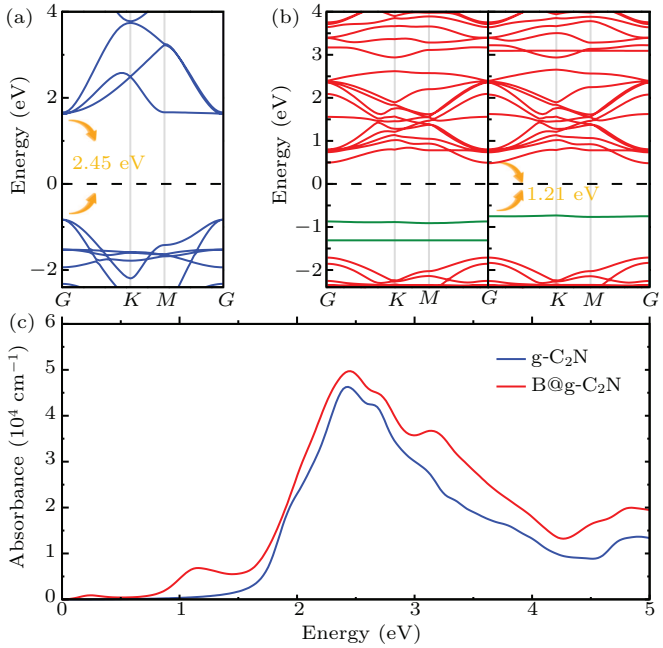


Fig. 2. The Band structures of (a) g-C_2N and (b) B/g-C_2N with spin up (left) and spin down (right). The Fermi level is set to 0 eV (dashed line). (c) The optical absorption spectra of g-C_2N and B/g-C_2N.

In order to achieve high-efficiency application in photocatalytic materials, wide and strong optical absorption in the optimal visible-light regions is naturally expected. Thus, we further investigate the optical absorption spectra for the g-C_2N and B/g-C_2N monolayers. As shown in Fig. 2(c), it is noted that the introduction of B atom is found to be further extended the absorption edge to the infrared light region and enhance the visiblelight absorption efficiency slightly, indicating that visible-light utilization of the B/g-C_2N is slightly more efficient than that of the pure g-C_2N monolayer.

3.2. N_2 molecule adsorbed on B/g-C_2N

As we all know, N_2 is adsorbed on catalysts via side-on and end-on adsorption patterns. Therefore, the interaction between N_2 and B/g-C_2N is investigated.

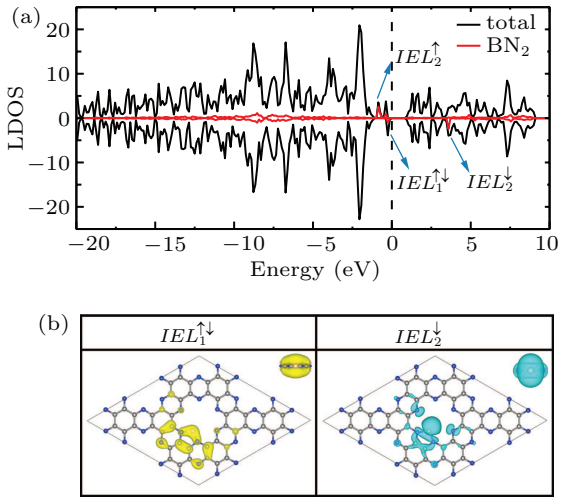


Fig. 3. (a) Spin-polarized local density of state (LDOS) of B/g-C_2N. (b) The charge density for the highest occupied molecular orbital (HOMO, labeled $IEL_1^{\uparrow\downarrow}$) and sixth-lowest unoccupied molecular orbital (LUMO+5, labeled $IEL_2^{\downarrow}$) of B/g-C_2N, where the isosurface value is set to be 0.001 e/Å^3. The gray, lightpink, and blue balls represent C, B and N atoms, respectively. The inset shows the orbital of moiety of BN_2 on side view.

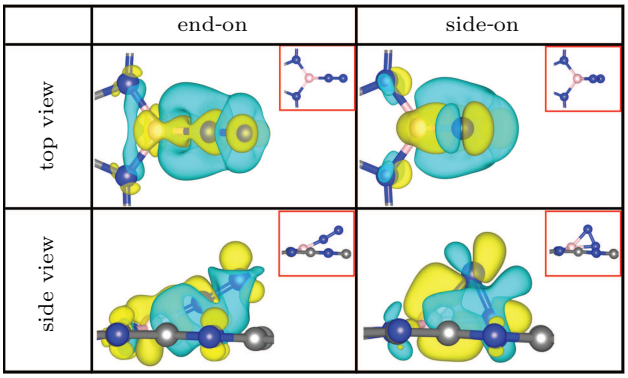


Fig. 4. Differential charge density of N_2 adsorbed on B/g-C_2N, where the isosurface value is set to be 0.02 e/Å^3. The charge accumulation and depletion are shown in yellow and cyan, respectively. The gray, lightpink, and blue balls represent C, B and N atoms, respectively.

Figure 3(a) shows the spin-polarized local density of state (LDOS) of B/g-C_2N. Figure 3(b) presents the partial charge density of the highest occupied molecular orbital (HOMO, labeled $IEL_1^{\uparrow\downarrow}$) and sixth-lowest unoccupied molecular orbital (LUMO+5, labeled $IEL_2^{\downarrow}$) of B/g-C_2N. The differential charge density of N_2 adsorbed on B/g-C_2N is plotted in Fig. 4. Adsorption energy ($E_{ads}^{N_2}$, in eV) and bond Length (d_{N-N}, in Å) of N_2 adsorbed on B/g-C_2N; Bader charge transfer ($\Delta\rho$) from B/g-C_2N to N_2; minimum energy reaction pathway (MERP); rate-limiting step (RLS) and onset potential (U, in units of V) for the electrocatalytic reaction of N_2 reduction to NH_3 on B/g-C_2N are also listed in Table 1. The shapes of HOMO and LUMO+5 of the moiety of BN_2 are similar to π orbital (Fig. 3), indicating that it has possibility to adsorb N_2 via side-on adsorption. This is because there are the better hybridization between N_2 and moiety of BN_2. Due to the fact that N_2 molecule has a lone pair of electrons and the moiety of

BN_2 has partially occupied π orbitals, it can be expected that the interaction between N_2 and BN_2 is "acceptance-donation" mechanism. As shown in Fig. 4, the charge density difference of B/g-C_2N adsorbed N_2 is calculated to clarify the interaction between B/g-C_2N and N_2. Obviously, the "acceptance-donation" process is found here, in which charge accumulation and depletion can be observed for both N_2 molecule and B/g-C_2N, indicating that the N_2 cannot only accept electrons from B/g-C_2N, but also donate electrons to B/g-C_2N. Clearly, compared to donate electrons, N_2 tends to accept electrons from B/g-C_2N, at the same time, N_2 with side-on adsorption pattern can accept more electrons than that of end-on adsorption pattern (Fig. 4), making the bond length of N_2 for side-on pattern (1.20 Å) is longer than that of end-on pattern (1.13 Å). The Bader charge analysis also confirms this conclusion. Table 1 shows that the N_2 gains $0.73|e|$ and $0.39|e|$ from B/g-C_2N for side-on and end-on patterns, respectively. The increase of N≡N bond length implies the activation of the inert N≡N triple bond. We note that the better orbital hybridization can be achieved when N_2 is adsorbed onto B/g-C_2N with side-on pattern. Therefore, the energy released by side-on adsorption pattern should be more than that released by end-on adsorption pattern. However, due to the "acceptance-donation" interaction mechanism, more electrons are obtained by $1\pi^*$ antibonding orbital of N_2 for side-on adsorption pattern, as mentioned in our previous work,[49] which will lead to the longer N≡N bond length. Thus, the energy released by side-on pattern is less than that released by end-on pattern, because most of the energy is used to activate the N≡N triple bond. As is expected, as shown in Table 1, the adsorption of N_2 to B/g-C_2N is an exothermic process with the adsorption free energy of −0.02 eV and −0.82 eV for side-on and end-on adsorption patterns, respectively.

Table 1. Adsorption energy ($E_{ads}^{N_2}$, in eV) and bond length (d_{N-N}, in Å) of N_2 adsorbed on B/g-C_2N; Bader charge transfer ($\Delta\rho$) from B/g-C_2N to N_2; minimum energy reaction pathway (MERP); rate-limiting step (RLS) and onset potential (U, in V) for the electrocatalytic reaction of N_2 reduction to NH_3 on B/g-C_2N.

Adsorption pattern	$E_{ads}^{N_2}$ (ΔG_{N_2})	d_{N-N} ($\Delta\rho$)	MERP	RLS	U
End-on	−1.40 (−0.82)	1.13 (0.39)	pathway V	$^*N–NH_2 \rightarrow {}^*N$	0.74
Side-on	−0.57 (−0.02)	1.20 (0.73)	pathway V	$^*N–{}^*NH \rightarrow {}^*N–{}^*NH_2$	0.07

3.3. Electrocatalytic NRR

Generally, as shown in Fig. 5, the photocatalytic reaction of NRR on B/g-C_2N will follow five possible reaction pathways no matter whether adsorption configuration is end-on or side-on, and the reaction process involve six net proton coupled electron transfer steps (PCETSs). Take the end-on adsorption configuration as an example, the five possible reaction pathways include: (I) The initial three PCETSs focus on the same N atom far away from B/g-C_2N (as shown in Fig. 4), forming the $^*N–NH$, $^*N–NH_2$ and $^*N$ intermediate, and then the first NH_3 is generated, the remaining three PCETSs form the $^*NH$, $^*NH_2$ and $^*NH_3$ intermediate in turn, and the second NH_3 is finally release: $^*N–NH \rightarrow {}^*N–NH_2 \rightarrow {}^*N + NH_3 \rightarrow {}^*NH \rightarrow {}^*NH_2 \rightarrow {}^*NH_3$ (the red one in Fig. 5). (Ⅱ) The initial four PCETSs form the $^*N–NH$, $^*N–NH_2$, $^*NH–NH_2$ and $^*NH$ intermediate and generate the first NH_3, the rest two PCETSs form the $^*NH_2$ and $^*NH_3$ intermediate and generate another NH_3: $^*N–NH \rightarrow {}^*N–NH_2 \rightarrow {}^*NH–NH_2 \rightarrow {}^*NH + NH_3 \rightarrow {}^*NH_2 \rightarrow {}^*NH_3$ (the purple one in Fig. 5). (Ⅲ) The initial five PCETSs form the $^*N–NH$, $^*N–NH_2$, $^*NH–NH_2$, $^*NH_2–NH_2$ and $^*NH_2$ intermediate and generate the first NH_3, the last PCETS generate another NH_3: $^*N–NH \rightarrow {}^*N–NH_2 \rightarrow {}^*NH–NH_2 \rightarrow {}^*NH_2–NH_2 \rightarrow {}^*NH_2 + NH_2 \rightarrow {}^*NH_3$ (the green one in Fig. 5). (IV) The initial fourth PCETSs form the $^*N–NH$, $^*NH–NH$, $^*NH–NH_2$ and $^*NH$ intermediate and generate the first NH_3, the last two PCETSs form the $^*NH_2$ and $^*NH_3$ intermediate and generate another NH_3: $^*N–NH \rightarrow {}^*NH–NH \rightarrow {}^*NH–NH_2 \rightarrow {}^*NH + NH_3 \rightarrow {}^*NH_2 \rightarrow {}^*NH_3$ (the magenta one in Fig. 5). (V) The initial five PCETSs form the $^*N–NH$, $^*NH–NH$, $^*NH–NH_2$, $^*NH_2–NH_2$ and $^*NH_2$ intermediate and generate the first NH_3, the last PCETS generate another NH_3: $^*N–NH \rightarrow {}^*NH–NH \rightarrow {}^*NH–NH_2 \rightarrow {}^*NH_2–NH_2 \rightarrow {}^*NH_2 + NH_3 \rightarrow {}^*NH_3$ (the blue one in Fig. 5).

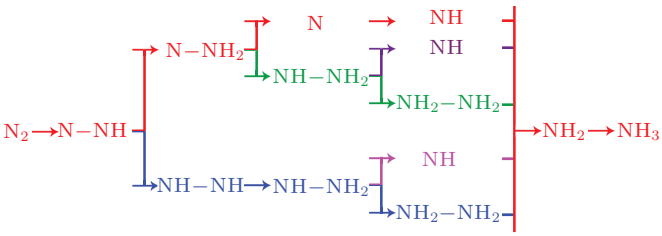


Fig. 5. Proposed schematic elementary reactions for N_2 reduction to NH_3 on B/g-C_2N. The red, purple, green, magenta and blue lines represent the reaction pathways I, Ⅱ, Ⅲ, Ⅳ, and Ⅴ, respectively.

Gibbs free energy change (ΔG) in each reaction process is generally used to evaluate the catalytic performance of B/g-C_2N for the reduction of N_2 to NH_3. The ΔG diagrams for the NRR on B/g-C_2N for the five reaction pathways are shown in Fig. 6. Providing that N_2 is adsorbed on B/g-C_2N via end-on adsorption pattern, as shown in Fig. 6(a), the adsorption Gibbs free energy is negative (−0.82 eV), indicating high binding strength between N_2 and B/g-C_2N. Regarding the reaction pathway I (the red one in Figs. 5 and 6(a)), the hydrogenation of $^*N–NH_2$ to $^*N$ is the RLS, requiring a high energy

input (1.01 eV), which corresponds to the third PCETSs (*N–$NH_2 + H^+/e^- \rightarrow {}^*N + NH_3$). For the remaining four reaction pathways, the RLS is the hydrogenation of *N–N to *N–NH, and the corresponding ΔG is about 0.74 eV. Therefore, the minimum free-energy pathway is the second-to-fifth reaction pathways.

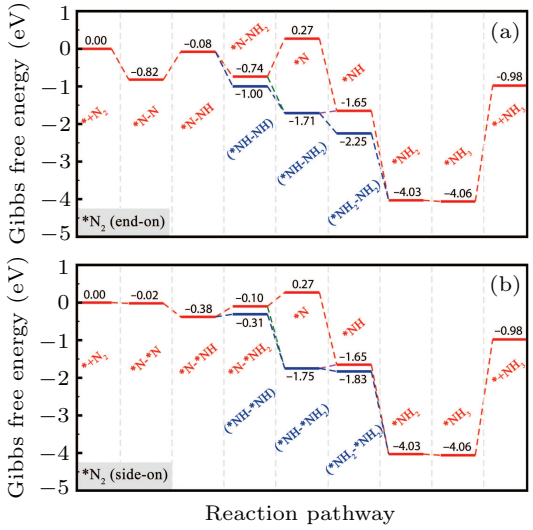


Fig. 6. Gibbs free-energy change (ΔG) for N_2 reduction to NH_3 on B/g-C_2N through (a) end-on and (b) side-on pattern. Here * denotes the catalyst (B/g-C_2N). The red, purple, green, magenta and blue lines represent the reaction pathways I, Ⅱ, Ⅲ, Ⅳ and Ⅴ, respectively, as shown in Fig. 5. The energy of the entrance, including the isolated B/g-C_2N and free N_2 molecule, is set to zero as the reference.

As for N_2 adsorbed on B/g-C_2N via side-on adsorption pattern, the adsorption Gibbs free energy is negative (−0.02 eV), which is smaller than that of the end-on adsorption pattern. We notice that, for the first PCETSs, the side-on adsorption pattern is exothermic (−0.36 eV), while the end-on adsorption pattern is endothermic reaction (0.74 eV). For the reaction pathway I (the red one in Figs. 5 and 6(b)), the RLS is the hydrogenation of *N–$^*NH_2$ to *N, which is the same with the end-on adsorption pattern, and requires a high energy input (0.37 eV). The RLS of reaction pathway Ⅱ and Ⅲ are the hydrogenation of *N–*NH to *N–$^*NH_2$ with ΔG=0.28 eV. As for the reaction pathway Ⅳ and Ⅴ, the RLS are the hydrogenation of *NH–$^*NH_2$ to *NH with $\Delta G = 0.10$ eV and the hydrogenation of *N–*NH to *NH–*NH with $\Delta G = 0.07$ eV, respectively. The fifth reaction pathway (the blue one in Figs. 5 and 6(b)) has the minimum free-energy (0.07 eV), so it is concluded that the reaction pathway Ⅴ (i.e., enzymatic mechanism) is the minimum free-energy pathway. Consequently, we come to a conclusion that, for the side-on adsorption pattern, the onset potential only requires 0.07 V to eliminate the increase in Gibbs free energy, and the NRR reaction can be carried out smoothly. Such a smaller onset potential means that it is very easy for nitrogen reduction into ammonia under ambient conditions.

In order to study the dynamic process of NRR, the activation barriers of six kinds of PCETSs are calculated. In the case of classical chemical reactions, the TS is located with a zero charge-electron balance during the chemical process. For the NRR, the production of adsorbed *AH intermediate state is generated by: $^*A + H^+ + e^- \rightarrow {}^*AH$, and the chemical species A is adsorbed on a catalytic surface, such as N_2, N_2H, etc. However, the calculation of TS in such a chemical reaction is difficult due to the dissociated proton. Based on this, Janik and co-workers[43] proposed the analogous hydrogenation reaction in which both A and H are adsorbed on the catalyst surface and react to produce the *AH intermediate state via: $^*A + {}^*H \rightarrow {}^*AH$. Finally, based on the Marcus theory and the Butler–Volmer theory, the Gibbs free activation barrier of the reduction reaction of *A, ΔG_{react}, can be approximated as $G_{\text{react}}(U) = G_0 + \beta FU$, where G_0 is the calculated activation barrier for the hydrogenation reaction of *A, β is the symmetry coefficient (approximately 0.5), F is the Faraday constant, and U is the applied electrode potential.[13]

For every PCETSs, the chemical species A and the H atom are adsorbed on the B atom and N atom of the B/g-C_2N as the initial reactant, respectively. Figure 7 shows the structures and Gibbs free energies of the transition states (TSs) in the minimum energy pathway (i.e., reaction pathway Ⅴ) for the N_2 reduction to NH_3 with side-on adsorption configuration. It is easy to find that the maximum Gibbs free-energy barrier of 0.50 eV lies in the second PCETSs (*N–$^*NH + H^+/e^- \rightarrow {}^*NH$–*NH), and the corresponding transition state is TS2 (*N–*NH+*H), in accordance with the RLS of Gibbs free energy change (the blue one in Fig. 6(b)). As for the rest of the reaction processes, the Gibbs free energy barriers are all lower than 0.5 eV. The transition states of TS1, TS4 and TS5 generate the *N–*NH, $^*NH_2$–$^*NH_2$ and $^*NH_2$ intermediate species, respectively, with the corresponding Gibbs free energy barriers of only 0.06, 0.12, and 0.01 eV.

Interestingly, as shown in Fig. 2, the doping of B atom into g-C_2N leads to the introduction of impurity energy levels, which further extend the absorption edge to the infrared light region and enhance the visiblelight absorption efficiency slightly. The maximum absorption peak is about located in 2.45 eV, indicating that B/g-C_2 possess outstanding ability to absorb certain energies of visible light. At the same time, the smaller peak located at 1.20 eV originates from the doping of B atom. Due to the fact that the maximum Gibbs free energy barrier is only 0.50 eV, photon energy absorbed by the B/g-C_2N is enough to overcome this barrier, highlighting the outstanding catalytic performance of B/g-C_2N for NRR.

As seen from Fig. 8, the Bader charge analysis of the whole reaction shows that the electrons transferring to N_2 mainly come from the moiety of BN_2 of B/g-C_2N (moiety-1) when N_2 is initially adsorbed, no matter whether it is end-on adsorption or side-on adsorption, indicating that the BN_2 plays the key role to capture active N_2. Thereinto more electrons are

transferred from B to N_2 than from two N atoms of BN_2 to N_2, because the occupied orbital (HOMO) and unoccupied orbital (LUMO+5) of BN_2 consist largely of s, p_x (p_y) and p_z orbitals of B atom (Fig. 8(a)). In addition, N_2 direct contacts with B atom (Fig. 4). However, as shown in Fig. 8(b), in the course of the reaction, the BN_2 works as a transportation center to move the electrons of other parts of B/g-C_2N (moiety-2) which acts as a electron reservoir to the N_xH_y (moiety-3), because the amounts of electrons for moiety-1 almost do not change during the whole reaction, while the change trend of the amounts of electrons for moiety-3 is just opposite to that of the moiety-2. It is found that, as shown in the bottom row of Fig. 8(b), the electron transfer of B atom in moiety-1 is completely consistent with that of moiety-1, at the same time, the amounts of electrons for both the N atoms in moiety-1 remain approximately constant. Therefore, it is concluded that the introduction of B atom makes g-C_2N only attract N_2 appropriately, but also carry the electrons of reservoir to the N_2 effectively.

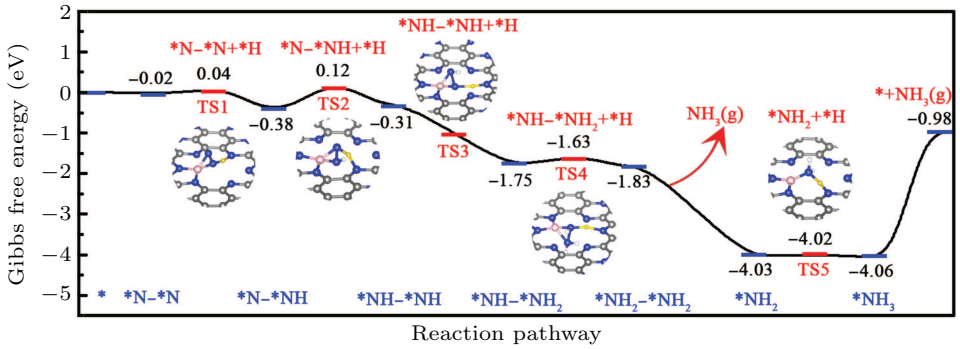


Fig. 7. Minimum energy pathway for N_2 reduction into NH_3 catalysed by B/g-C_2N through side-on pattern. The energy of the entrance, including the isolated B/g-C_2N and free N_2 molecule, is set to zero as the reference. The structures of the transition states (TSs) are indicated. The gray, lightpink, blue and white balls represent C, B, N and H atoms, respectively. The reactive hydrogen atom during the N_2 electroreduction is highlighted in golden in each step.

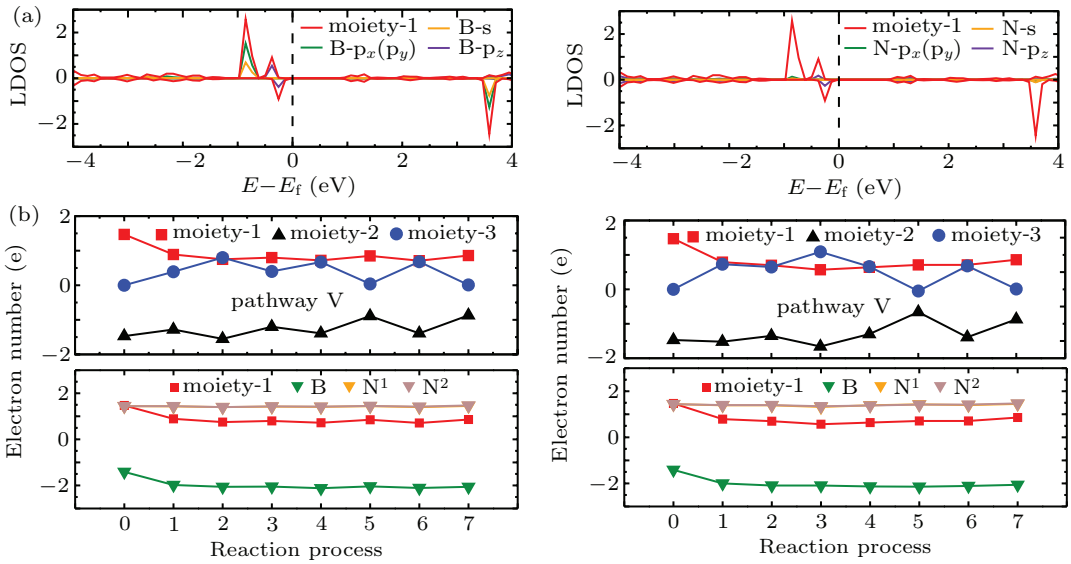


Fig. 8. (a) Spin-polarized local density of state (LDOS) of the moiety of BN_2. (b) Charge variation of the three moieties along the MERP (reaction pathway V) of N_2 with end-on (left) and side-on (right) adsorption configuration. The moiety-1, moiety-2 and moiety-3 represent BN_2 of B/g-C_2N, other parts of B/g-C_2N and adsorbed N_2, respectively. N^1 and N^2 are the N atom which bond to B atom. Reaction process 0, 1, 2, 3, 4, 5, 6, 7 represent the isolated state, N_2 adsorption reaction, initial, second, third, fourth, fifth and sixth protonation reaction, respectively.

In order to find out the origin of activity of B/g-C_2N, the local density of states (LDOS) of free N_2 molecule and B/g-C_2N adsorbed N_2 molecule are calculated, as shown in Fig. 9. The molecular orbitals of free N_2 molecule mainly include 2σ, $2\sigma^*$, 1π, 3σ, $1\pi^*$, and $3\sigma^*$ molecular orbitals. When N_2 is adsorbed on B/g-C_2N, the molecular orbitals of N_2 will hybridize with the HOMO and LUMO of moiety-1 of B/g-C_2N intensively, as shown in Figs. 9(b)–9(c). For the end-on adsorption pattern, the $1\pi^*$ orbital of N_2 can accept electrons from the HOMO of moiety-1 of B/g-C_2N, leading to the $1\pi^*$ orbital being partially occupied, and the $2\sigma^*$, 1π, 3σ orbitals of N_2 can donate the electrons to the LUMO of moiety-1 of B/g-C_2N, resulting in the decreases of their strength, which further confirm the "acceptance-donation" interaction mechanism. The Bader charge analysis shows that N_2 will get $0.39|e|$ net charge from B/g-C_2N (shown in Table 1).

As for side-on adsorption pattern, the $2\sigma^*$, 1π, 3σ orbitals have also changed and their strength also decreases, the difference is that the degree of the ionization of 1π orbital

and the filling of $1\pi^*$ orbital are stronger, in agreement with our previous research.[49] From the Bader charge analysis, as shown in Table 1, it is found that N_2 can get $0.73|e|$ net charge from B/g-C_2N, which means that the $1\pi^*$ orbital of N_2 can accept more electrons from the HOMO of moiety-1 of B/g-C_2N in side-on adsorption pattern than that of end-on adsorption pattern, that is why the d_{N-N} of the side-on adsorption pattern is longer than that of the end-on adsorption pattern. The longer d_{N-N} means the more active of N_2. Thus, the catalytic performance of B/g-C_2N with the side-on pattern of N_2 is the best reaction pathway.

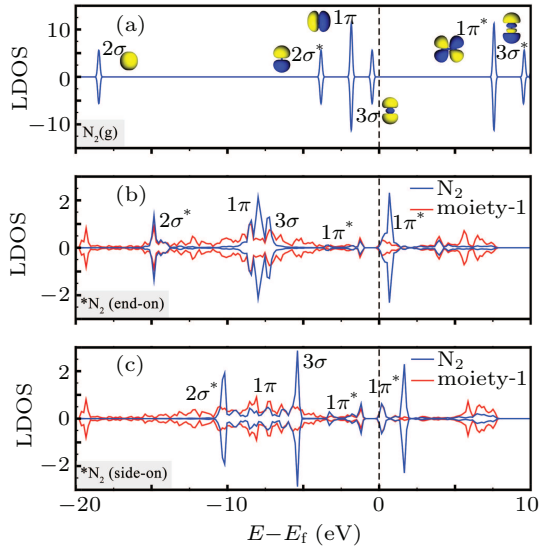


Fig. 9. Spin-polarized local density of state (LDOS) of (a) free N_2 molecule, N_2 adsorbed on B/g-C_2N with (b) end-on pattern and (c) side-on pattern. The blue and red lines represent the total LDOS of N_2 and BN_2 of B/g-C_2N (moiety-1), respectively. The Fermi level is set to 0 eV.

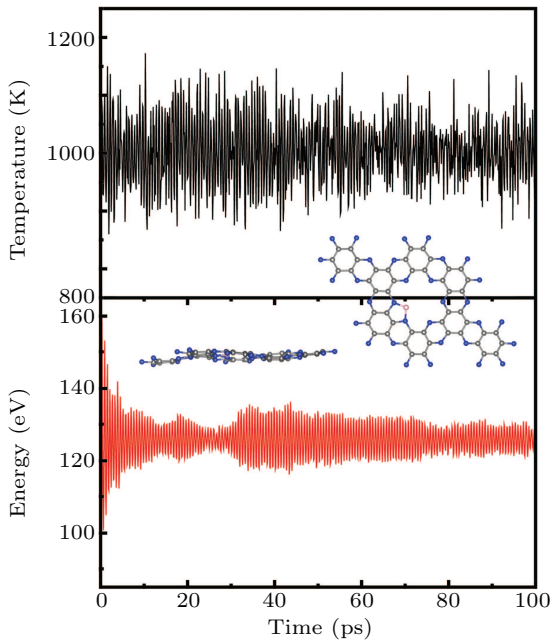


Fig. 10. Variations of temperature and total energy of against the time for the molecular dynamics simulation of B/g-C_2N, carried out with a universal force field as implemented in Forcite code. Insets are top and side views of the snapshot of atomic configuration. The simulation is run under 1000 K for 100 ps with time steps of 2 fs.

Moreover, the stability of catalyst is also very important to the application in realistic case. We have examined the stability using AIMD simulations. As shown in Fig. 10, when temperature increases to 1000 K, the structure of B/g-C_2N is a slight of distortion in vertical plane, still a horizontal surface is not greatly changed, showing the outstanding thermostability.

4. Conclusions

In summary, we have demonstrated that B/g-C_2N can be a excellent photocatalyst for N_2 reduction to NH_3 by performing the first-principles calculations. The calculated results indicate that the introduction of B atom to g-C_2N can not only maintain and improve slightly the optical absorption in the visible-light region relative to the pure g-C_2N, but also act as capture and activate center of N_2 through the acceptance-donation mechanism. The low thermodynamics reaction free energy of 0.07 eV and free energy barrier of 0.50 eV, far below the photon energy absorbed by the B/g-C_2N, making B/g-C_2N as photocatalyst holds great potential for the reduction for the N_2 fixation. In addition, the strong binding energy offers high probability in terms of experimental synthesis. Furthermore, B/g-C_2N shows high thermal stability even though the temperature up to 1000 K.

Acknowledgement

The computation is performed in the Supercomputer Center of Ningbo University.

References

[1] Rosca V, Duca M, de Groot M T and Koper M T 2009 *Chem. Rev.* **109** 2209
[2] Licht S, Cui B, Wang B H, Li F F, Lau J and Liu S Z 2014 *Science* **345** 637
[3] Smil V 1999 *Nature* **400** 415
[4] Service R F 2014 *Science* **345** 610
[5] Van der Ham C J M, Koper M T M and Hetterscheid D G H 2014 *Chem. Soc. Rev.* **43** 5183
[6] Oshikiri T, Ueno K and Misawa H 2016 *Angew. Chem.* **128** 4010
[7] Kitano M, Inoue Y, Yamazaki Y, Hayashi F, Kanbara S, Matsuishi S, Yokoyama T, Kim S W, Hara M and Hosono H 2012 *Nat. Chem.* **4** 934
[8] Seh Z W, Kibsgaard J, Dickens C F, Chorkendorff I, Nørskov J K and Jaramillo T F 2017 *Science* **355** eaad4998
[9] Banerjee A, Yuhas B D, Margulies E A, Zhang Y B, Shim Y, Wasielewski M R and Kanatzidis M G 2015 *J. Am. Chem. Soc.* **137** 2030
[10] Bao D, Zhang Q, Meng F L, Zhong H X, Shi M M, Zhang Y, Yan J M, Jiang Q and Zhang X B 2017 *Adv. Mater.* **29** 1604799
[11] Sun K, Moreno-Hernandez I A, Schmidt W C, Zhou X, Crompton J C, Liu R, Saadi F H, Chen Y, Papadantonakis K M and Lewis N S 2017 *Energy Environ. Sci.* **10** 987
[12] Montoya J H, Tsai C, Vojvodic A and Nørskov J K 2015 *Chem. Sus. Chem.* **8** 2180
[13] Azofra L M, Li N, MacFarlane D R and Sun C 2016 *Energy Environ. Sci.* **9** 2545
[14] Yu X, Han P, Wei Z, Huang L, Gu Z, Peng S, Ma J and Zheng G 2018 *Joule* **2** 1610
[15] Guo C, Ran J, Vasileff A and Qiao S Z 2018 *Energy Environ. Sci.* **11** 45
[16] Qiu W, Xie X Y, Qiu J, Fang W H, Liang R, Ren X, Ji X, Cui G, Asiri A M, Cui G, Tang B and Sun X 2018 *Nat. Commun.* **9** 3485

[17] Tao H, Choi C, Ding L X, Jiang Z, Han Z, Jia M, Fan Q, Gao Y, Wang H, Robertson A W, Hong S, Jung Y, Liu S and Sun Z 2019 *Chem* **5** 204

[18] Qu L, Liu Y, Baek J B and Dai L 2010 *ACS Nano* **4** 1321

[19] Liu J, Liu Y, Liu N, Han Y, Zhang X, Huang H, Lifshitz Y, Lee S T, Zhong J and Kang Z 2015 *Science* **347** 970

[20] Xu Y, Kraft M, Xu R 2016 *Chem. Soc. Rev.* **45** 3039

[21] Yang S, Feng X, Wang X and Müllen K 2011 *Angew. Chem.* **123** 5451

[22] Zheng Y, Jiao Y, Zhu Y, Li L H, Han Y, Chen Y and Qiao S Z 2014 *Nat. Commun.* **5** 3783

[23] Xia Z 2016 *Nature Energy* **1** 16155

[24] He J, Wang N, Yang Z, Shen X, Wang K, Huang C and Li Y 2018 *Energy Environ. Sci.* **11** 2893

[25] Zhao Z, Li M, Zhang L, Dai L and Xia Z 2015 *Adv. Mater.* **27** 6834

[26] Ran J, Guo W, Wang H, Zhu B, Yu J and Qiao S Z 2018 *Adv. Mater.* **30** 1800128

[27] Lu Z, Chen G, Siahrostami S, Chen Z, Liu K, Xie J and Jaramillo T F 2018 *Nature Catalysis* **1** 156

[28] Xie J, Zhao X, Wu M, Li Q, Wang Y and Yao J 2018 *Angew. Chem. Int. Ed.* **57** 9640

[29] Ling C, Niu X, Li Q, Du A and Wang J 2018 *J. Am. Chem. Soc.* **140** 14161

[30] Li Y Y, Ma S F, Zhou B X, Huang W Q, Fan X X, Li X F, Li K and Huang G F 2019 *J. Phys. D: Appl. Phys.* **52** 105502

[31] Li Y Y, Si Y, Han E X, Huang W Q, Hu W Y, Pan A L, Fan X X and Huang G F 2020 *J. Phys. D: Appl. Phys.* **53** 015502

[32] Li Y Y, Si Y, Zhou B X, Huang W Q, Hu W Y, Pan A L, Fan X X and Huang G F 2019 *Nanoscale* **11** 16393

[33] Yu S, Rao Y C and Duan X M 2017 *Chin. Phys. B* **26** 087301

[34] Liu J, Zhang Y H, Bai Z M, Huang Z A and Gao Y K 2019 *Chin. Phys. B* **28** 048101

[35] Chu Z Q, Gu X and Duan X M 2019 *Chin. Phys. B* **28** 128703

[36] Mahmood J, Lee E K, Jung M, Shin D, Jeon I Y, Jung S M and Park N 2015 *Nat. Commun.* **6** 6486

[37] Mahmood J, Li F, Jung S M, Okyay M S, Ahmad I, Kim S J and Baek J B 2017 *Nat. Nanotechnol.* **12** 441

[38] Zhang X, Chen A, Zhang Z, Jiao M and Zhou Z 2018 *J. Mater. Chem. A* **6** 11446

[39] Wang L, Zheng X, Chen L, Xiong Y and Xu H 2018 *Angew. Chem.* **130** 3512

[40] Zhang X, Chen A, Zhang Z and Zhou Z 2018 *J. Mater. Chem. A* **6** 18599

[41] Kresse G and Furthmüller J 1996 *Phys. Rev. B* **54** 11169

[42] Kresse G and Joubert D 1999 *Phys. Rev. B* **59** 1758

[43] Blöchl P E 1994 *Phys. Rev. B* **50** 17953

[44] Perdew J P, Chevary J A, Vosko S H, Jackson K A, Pederson M R, Singh D J and Fiolhais C 1992 *Phys. Rev. B* **46** 6671

[45] Perdew J P and Wang Y 1992 *Phys. Rev. B* **45** 13244

[46] Grimme S 2006 *J. Comput. Chem.* **27** 1787

[47] Heyd J, Scuseria G E and Ernzerhof M 2003 *J. Chem. Phys.* **118** 8207

[48] Henkelman G, Uberuaga B P and Jónsson H 2000 *J. Chem. Phys.* **113** 9901

[49] Nie X, Esopi M R, Janik M J and Asthagiri A 2013 *Angew. Chem. Int. Ed.* **52** 2459

[50] Rappe A K, Casewit C J, Colwell K S, Iii W A, Goddard and Skiff W M 1992 *J. Am. Chem. Soc.* **114** 10024

[51] Nørskov J K, Rossmeisl J, Logadottir A, Lindqvist L, Kitchin J R, Bligaard T and Jónsson H 2004 *J. Phys. Chem. B* **108** 17886

[52] Rossmeisl J, Logadottir A and Nørskov J K 2005 *Chem. Phys.* **319** 178

[53] Zhang H, Zhang X, Yang G and Zhou X 2018 *J. Phys. Chem. C* **122** 5291

[54] Zhang R, Li B and Yang J 2015 *Nanoscale* **7** 14062

[55] Zhu H R, Hu Y L, Wei S H and Hua D Y 2019 *J. Phys. Chem. C* **123** 4274